ISIJ International, Vol. 66 (2026), No. 9, pp. 1066–1071
https://doi.org/10.2355/isijinternational.ISIJINT-2026-079

Development of a Single-crystalline-like Texture in 316L Stainless Steel using a Novel Brick Scan Strategy in Laser-powder Bed Fusion

Ryosuke OZASA,[1,2] Ryota WATANABE,[1] Shogo HIRATA,[1] Takuya ISHIMOTO[1,3] and Takayoshi NAKANO[1,2]*

1) Division of Materials and Manufacturing Science, Graduate School of Engineering, The University of Osaka, 2-1 Yamadaoka, Suita, Osaka, 565-0871 Japan.
2) 3DPTec Integrated Center, The University of Osaka, 2-1 Yamadaoka, Suita, Osaka, 565-0871 Japan.
3) Aluminium Research Center, University of Toyama. Now at Titanium Research Center (TRC), University of Toyama, 3190, Gofuku, Toyama, Toyama, 930-8555 Japan.

(*Received March 31, 2026; Accepted July 2, 2026; Advance online published July 10, 2026; Published August 15, 2026*)

As the properties of metallic materials depend on their crystallographic texture, the development of a strong texture is essential for functional control. This study achieved a single-crystalline-like texture with a hierarchical microstructure in 316L stainless steel (316L SS) through laser-powder bed fusion (L-PBF). A conventional ±X-scan strategy (employing bi-directional scanning along the x-axis for all layers) afforded a unique microstructure in which two differently oriented grains (<001> and <011> along the z-axis) appeared alternately. On the other hand, a novel ±X-brick-scan strategy, which employs bi-directional scanning along the x-axis for all layers while shifting the laser irradiation position by half a pitch between layers, afforded a single-crystalline-like texture with <011> orientation along both the z- and y-axes. The difference in texture originates from the crystal growth direction. In the ±X-brick-scan strategy, the <001> growth direction was inclined by approximately ±45° from the z-axis, whereas it aligned parallel to the z-axis at the melt pool bottom in the ±X-scan strategy. Notably, this growth behavior does not fully correspond to the calculated heat-flow direction in the ±X-brick-scan case. These results suggest that the crystal growth direction in L-PBF is governed not only by heat flow, but also by additional factors such as interfacial energy.

KEY WORDS: crystallographic texture; crystal growth; microstructure; laser-powder bed fusion; 316L stainless steel.

1. Introduction

Additive manufacturing (AM) has attracted considerable attention for fabricating metallic materials. Laser-powder bed fusion (L-PBF), one of the AM techniques, can manufacture products of various shapes via the selective laser irradiation onto a powder bed of raw metal.[1–6] Owing to its unique temperature field created during the melting and solidification of metals, L-PBF can control material properties, including crystallographic texture,[7–12] solid solution,[13–15] and microstructures.[16–24] Such control of material properties has attracted significant attention in this technique.

L-PBF involves transient and local heating of a powder bed via laser beam irradiation at high speed, resulting in an extremely high thermal gradient (G), a high solidification rate (R) at the solid–liquid interface, and a resultant high cooling rate of approximately ~10^7 K/s, which cannot be achieved in conventional processes.[25] Notably, L-PBF generates a directional thermal gradient and resultant heat flow, which is one of the determinants of crystal growth direction.[7,8]

In case of 316L stainless steel (316L SS), a unique crystallographic lamellar microstructure (CLM) is often formed via L-PBF.[26–28] This microstructure comprises two types of grains, with the <011> and <100> orientations along the z-axis (building direction) stacked alternately. CLMs can be developed over a wide process window. However, the availability of a single-crystalline-like texture in 316L SS is limited. The "<001>-oriented texture" has been obtained under high energy density (ED) condition, owing to the small curvature of the melt pool bottom.[27] Moreover, the "<001>-oriented texture" along the z-axis was also developed via an ±XY-scan strategy,[28] suggesting that the scan strategy, namely the laser irradiation directions and patterns in each layer, is critical for tailoring crystallographic textures. As the functional properties of metallic materials vary significantly depending on the crystallographic orientation,

* Corresponding author: E-mail: nakano@mat.eng.osaka-u.ac.jp

controlling the texture is essential for functional control. In particular, the development of orientations other than the "<001>-oriented texture" enables further functional tailoring in 316L SS. This paper proposes a novel strategy for the development of a single-crystalline-like "$<011>_{//z}$-oriented texture" and discusses the formation behaviors of the crystallographic texture.

2. Materials and Methods

The feedstock 316L SS powder was obtained from EOS GmbH (Germany). The powder composition is presented in **Table 1**. The L-PBF process was conducted using the EOS M290 (EOS, Germany) system, where the laser power P, scanning speed v, scanning pitch d, and stacking thickness t were set in two ED conditions: 65.1 J/mm^3 (P = 250 W, v = 800 mm/s, d = 0.08 mm, and t = 0.06 mm) and 37.2 J/mm^3 (P = 250 W, v = 1 400 mm/s, d = 0.08 mm, and t = 0.06 mm). Samples with dimensions of 10 mm × 10 mm × 10 mm were fabricated in an Ar atmosphere by employing two types of scan strategies, as illustrated in **Fig. 1**: a conventional ±X-scan with bi-directional scanning in one direction for all layers (Fig. 1(a)) and our designed strategy, ±X-brick-scan, which involves bi-directional scanning in one direction for all layers while shifting the laser irradiation position by half a pitch between layers (Fig. 1(b)). We hypothesized that suppressing the epitaxial growth of <001> along the z-axis at the center part near the melt pool bottom observed in the ±X-scan[26–28] would afford a single-crystalline-like texture. The continuous and regular arrangement of the melt pools along the z-axis contributed to this unique crystal growth in CLM. Thus, ±X-brick-scan was proposed to suppress <001> growth along the z-axis by shifting the laser irradiation position by half a pitch between the layers. The ED of 65.1 J/mm^3 was applied to both scan strategies (±X-scan and ±X-brick-scan samples), while the ED of 37.2 J/mm^3 was applied only to ±X-scan (±X-scan-L sample). The building direction was defined as the z-axis, and the direction perpendicular to both the x- and z-axes was set as the y-axis (90° direction) in this study, according to the ISO/ASTM 52900 standard terminology.

Table 1. Composition of 316L SS powder used in this study (wt.%).

Fe	Cr	Ni	Mn	Si	Mo	N	P	C	Cu	S
bal.	17.85	14.44	1.59	0.26	2.71	0.07	0.017	0.006	< 0.01	< 0.005

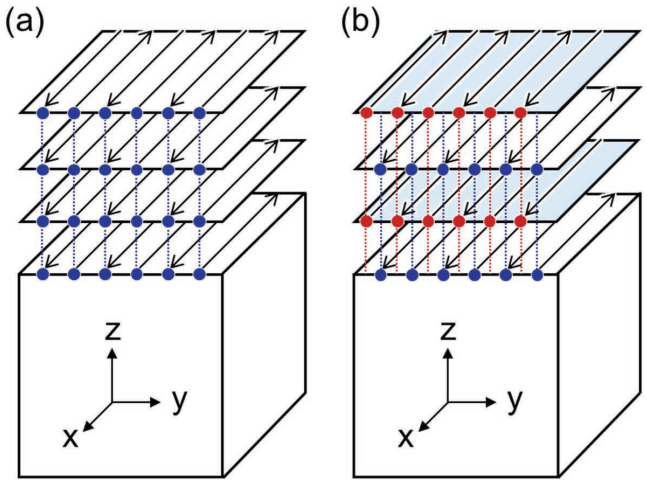

Fig. 1. Schematic of scan strategies applied in this study. (a) ±X-scan and (b) ±X-brick-scan. The dots and arrows indicate the positions of the laser center during each scan and the laser scanning direction, respectively.

The cross-sections of the samples were observed using a digital microscope (DSX1000, Olympus, Japan). The relative densities of the samples obtained in this study were above 99.9%. The microstructures of the samples were analyzed using scanning electron microscopy (SEM; JIB-4610F, JEOL, Japan). The crystallographic texture was examined by electron backscatter diffraction (EBSD; NordlysMax 3, Oxford Instruments, UK) with a measured step size of 2 μm and an accelerating voltage of 20 kV and analyzed using the AZtecHKL software (Oxford Instruments, UK). In the grain boundary analysis, misorientations of $2° \leq \theta < 15°$ were identified as low-angle grain boundaries (LAGBs) and misorientations of $\theta \geq 15°$ as high-angle grain boundaries (HAGBs). Mirror-polished samples were used for SEM-EBSD observations, while samples chemically etched with hydrofluoric acid were used for digital microscopy and SEM-secondary electron (SEM-SE) studies. The yz-plane perpendicular to the x-axis of the samples was observed in the microstructure.

A finite-element thermal diffusion simulation (COMSOL Multiphysics 5.5, COMSOL Inc., USA) was performed to investigate the directional distribution of heat flow using the previously established method.[8] The thermophysical properties of the materials used in the simulation were calculated using the JMatPro software, as presented in **Table 2**.

3. Results and Discussion

Figure 2 shows the cross-section of the yz-plane of each sample. While no defects are observed in Figs. 2(b) and 2(c), slight defects are observed in Fig. 2(a). The manufacturing proceeded from left to right within a layer, as the melt pool was partially overwritten by the neighboring right track. The melt pool was formed at the same y-position (Figs. 2(a), 2(b)) in the ±X-scan-L and ±X-scan and the alternate y-positions for each layer (Fig. 2(c)) in the ±X-brick-scan.

Figure 3 shows the texture of each sample in the yz-plane. The projections of the inverse pole figure maps along the z- and x-axes are illustrated in Figs. 3(a)–3(c) and Figs. 3(e)–3(g), respectively. The ±X-scan-L formed a weak texture without a preferred orientation (Figs. 3(a), 3(e), 3(h)).

Table 2. Physical and thermophysical parameters in the thermal diffusion simulation.

Physical parameters	Unit	Value
Density	g/cm^3	8.024
Thermal conductivity	W/m·K	10
Specific heat	J/kg·K	705
Latent heat of fusion	kJ/kg	234
Solidus temperature	K	1 661
Liquidus temperature	K	1 706

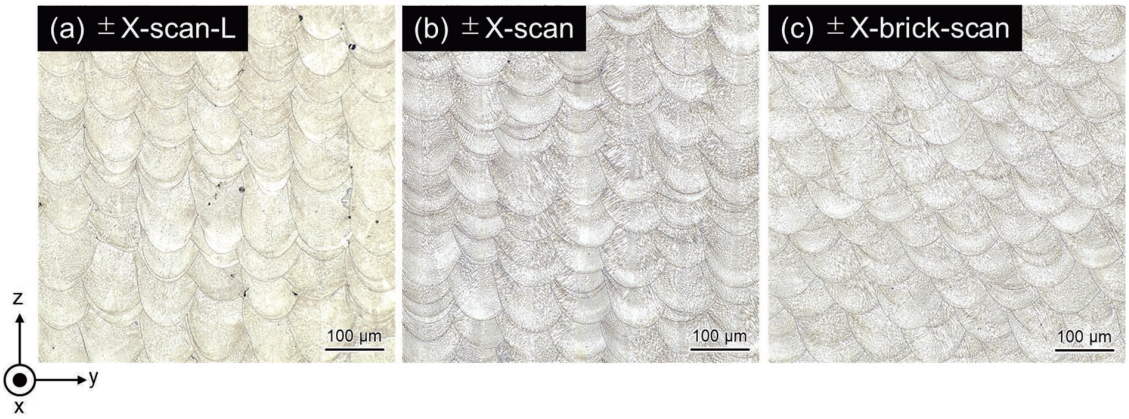

Fig. 2. Digital microscope images of each sample observed for the *yz*-plane. (a) ±X-scan-L, (b) ±X-scan, and (c) ±X-brick-scan.

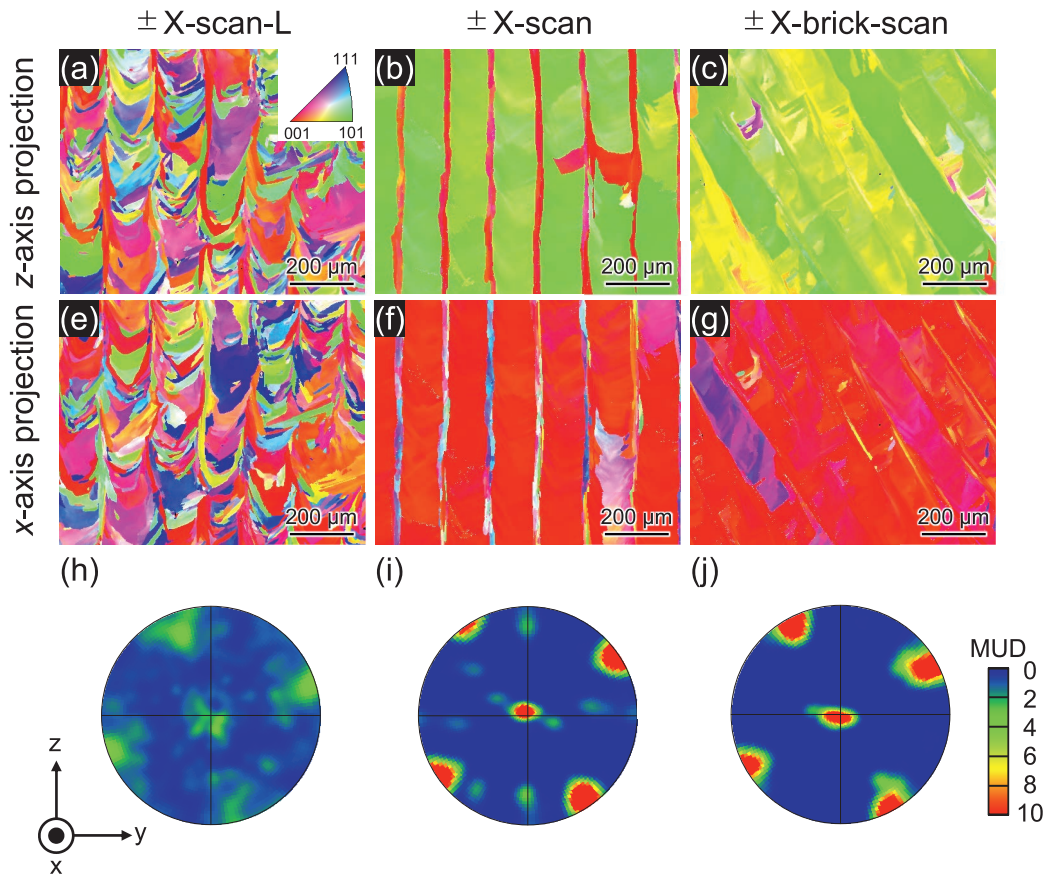

Fig. 3. Crystal orientation maps for the *yz*-plane obtained from each sample. Inverse pole figure maps projected along the *z*-axis and *x*-axis of the samples manufactured by (a, e) ±X-scan-L, (b, f) ±X-scan, and (c, g) ±X-brick-scan. Pole figures for {001} of the samples fabricated by (h) ±X-scan-L, (i) ±X-scan, and (j) ±X-brick-scan.

The ±X-scan formed a CLM composed of a main-layer and a sub-layer with different crystal orientations (Figs. 3(b), 3(f), 3(i)), as was observed in previous studies.[26–28] The crystal orientations with <001> and <011> were preferentially formed along the z-axis in the main- and sub-layers. Notably, the ±X-brick-scan suppressed the formation of the <001>-oriented sub-layer and promoted the growth of <011> along the z-axis, resulting in the formation of a single-crystalline-like $<011>_{//z}$-oriented texture (Figs. 3(c), 3(g), 3(j)). This is the first study to successfully control the texture by employing the brick scan strategy in 316L SS.

Figures 4(a)–4(c) show the grain boundary maps in each sample. The ±X-scan-L formed a high density of grain boundaries without preferred orientation and HAGBs were dominantly formed (Figs. 4(d), 4(e)). This is acceptable considering the formation of a polycrystal texture in this sample (Figs. 3(a)–3(c)). Compared with the ±X-scan-L, the ±X-scan showed a decreased grain boundary density and frequencies of the HAGBs. The ±X-brick-scan further suppressed the formation of HAGBs. It is noted that the directions of grain boundaries formed in ±X-brick-scan and ±X-scan were quite different. HAGBs aligned preferentially along the z-axis in the ±X-scan (Fig. 4(b)), whereas LAGBs were oriented along the axis diagonally up left and

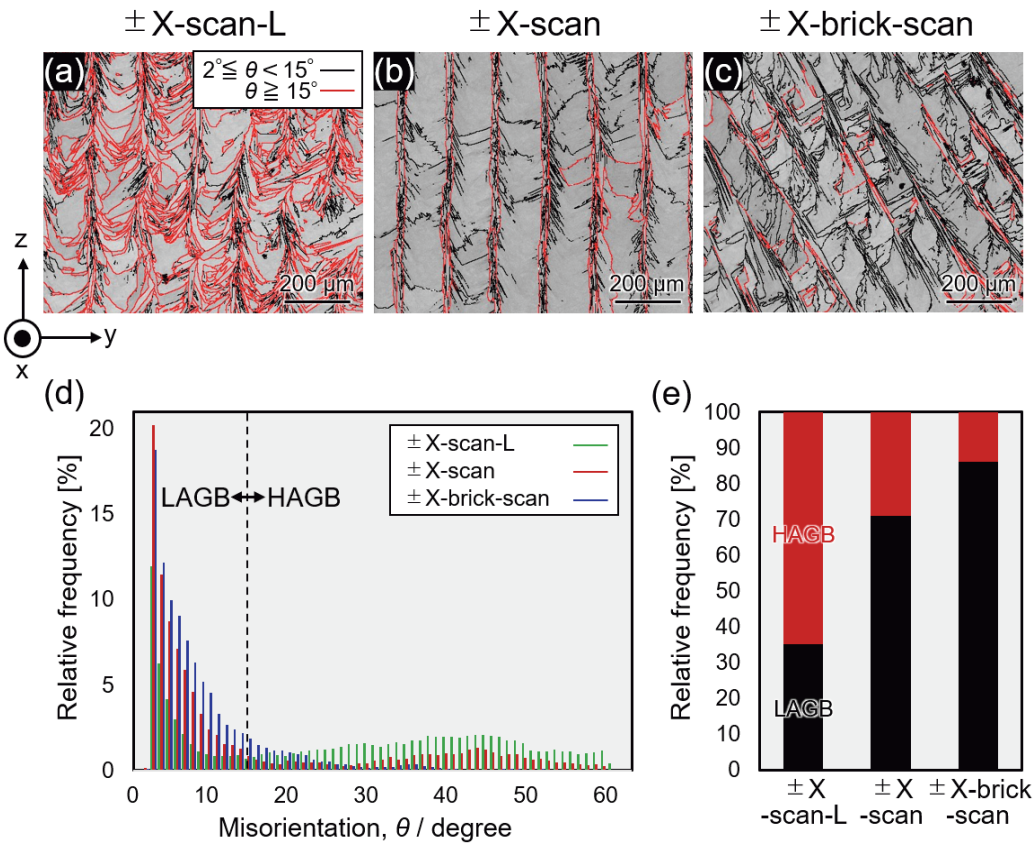

Fig. 4. Conditions of grain boundary distribution. (a-c) Grain boundary maps and (d) corresponding misorientation distributions. (e) Frequency of high angle grain boundary (HAGB) and low angle grain boundary (LAGB) of each sample.

the z-axis in the ±X-brick-scan (Fig. 4(c)). These results indicated that the crystallographic texture developed via different mechanisms in these scan strategies.

To discuss the texture evolution mechanism in the ±X-brick-scan, the corrosion-treated samples were observed by SEM. **Figure 5** shows the SEM-SE images overlaid with the traces of the melt pool edges observed in the *yz*-planes of the ±X-scan and ±X-brick-scan. In the L-PBFed 316L SS sample, constituent elements were segregated, and Cr and Mo are localized in the cellular wall.[29] Both elements exhibited superior corrosion resistance compared with the other constituent elements of 316L SS.[30,31] The present 316L SS samples also showed elemental segregation, as exhibited by submicron-ordered solidification microstructures (cells or dendrites without secondary dendrite arms). Because the etching rate differed between the Cr/Mo rich-cell and poor-intracellular walls, groove structures were carved on the surface of the samples via chemical etching. Thus, the cellular and intracellular regions appeared as bright and dark contrasts, respectively (Figs. 5(a)–5(h)). The elongated direction of the cellular microstructure corresponds to <001>, which is a favorable growth direction for metals with cubic systems.[32] Therefore, the difference between the alignment of the cellular microstructures of the two scan strategies reflects the difference in the crystal growth direction.

In the ±X-scan, the cellular microstructures align along the z-axis at the center part (red arrows) and the approximately ±45°-inclined axis against the z-axis (green arrows) at the area adjacent to the center part of each melt pool (Figs. 5(c), 5(f)). However, in the ±X-brick-scan, the cellular microstructures evolved only along an inclination of approximately ±45° against the z-axis (green arrows) in the left and right halves of each melt pool, without the z-axis-oriented growth of the cellular microstructures at the center part of each melt pool (Figs. 5(d), 5(h)).

Figure 6(a) shows a heat flow direction map on the *yz*-plane when the size of the melt pool is maximized, calculated by the thermal diffusion simulation. The laser parameters were set to those used in the ±X-scan and ±X-brick-scan. At the solid–liquid interface, illustrated by the black line, heat flow aligned along the z-axis near the center part of the melt pool, as illustrated in reddish colors and along the approximately ±45°-inclined axis against the z-axis in the left and right parts of the center part, as represented in greenish colors. Such a heat flow distribution calculated herein well corresponds to the elongated direction of the cellular microstructures in the ±X-scan (Fig. 5(c)). These results indicated that the crystal growth in the CLM can be governed by the heat flow direction. Once the crystal orientation has been determined, the main- and sub- layers inherit their orientation following the epitaxial growth from the adjacent (Fig. 5(e)) and underlying melt pools (Fig. 5(f)), leading to stable crystal growth along each crystal orientation. Thus, the unique texture developed in the ±X-scan can be triggered by the heat flow distribution and the following epitaxial crystal growth. Most importantly, although a similar heat flow is generated in the ±X-brick-scan, the growth direction of the cellular microstructure differs from that in the ±X-scan (Figs. 5(b), 5(d), 5(g), 5(h)). Hence, the growth of the cellular microstructures along the z-direction

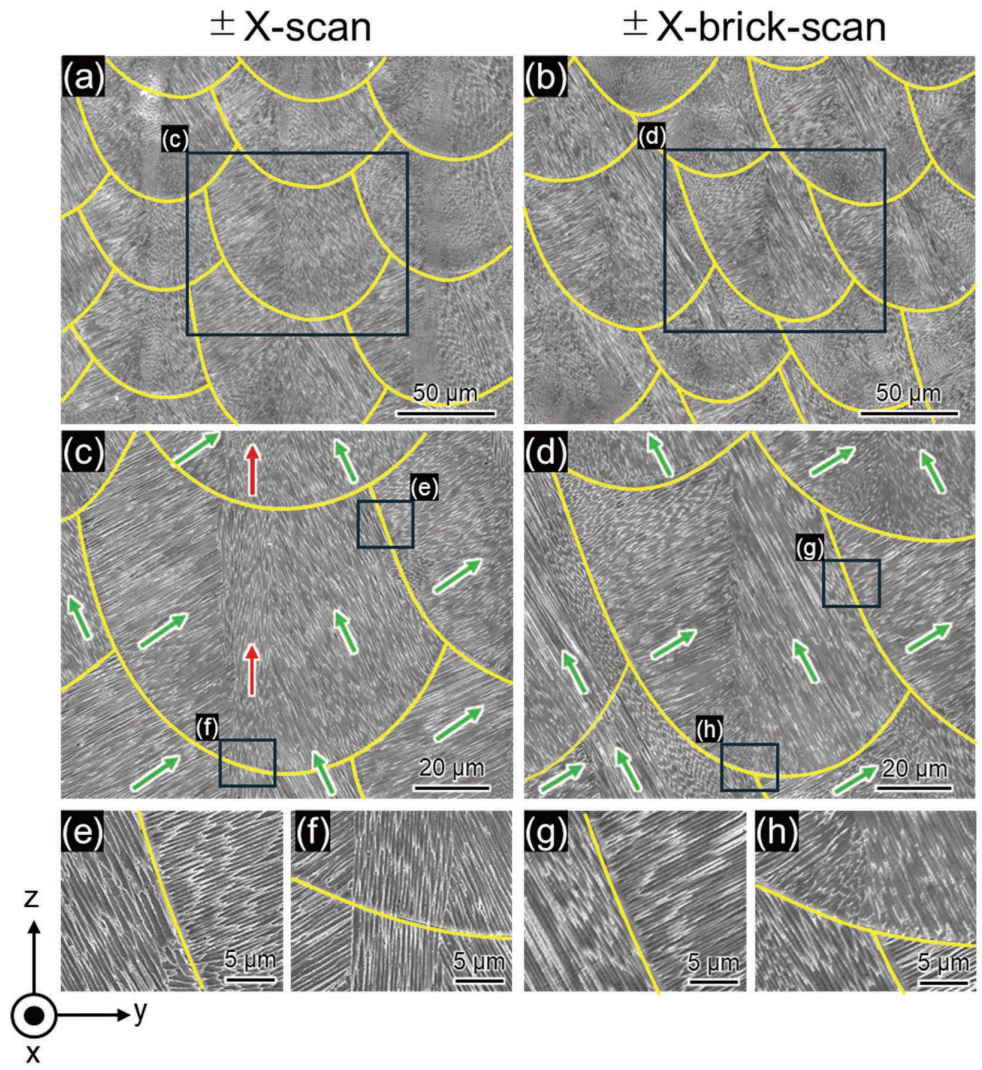

Fig. 5. SEM images showing the cell/dendrite microstructure on the *yz*-plane at different magnifications. The melt pool edges are highlighted with yellow lines and the arrows indicate the direction of microstructure (green: ±45°-oriented microstructures; red: vertically oriented microstructures).

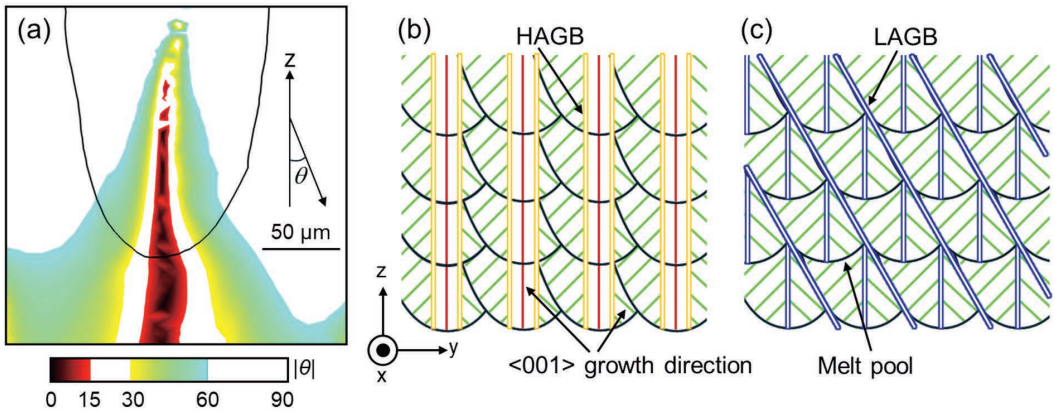

Fig. 6. Heat flow dependent- and independent-development of cell/dendrite microstructure of 316L SS. (a) Color map of heat flow direction on *yz*-plane of 316L SS. Schematics of the development of microstructures fabricated via (b) ±X-scan and (c) ±X-brick-scan. The melt pool edges are represented with black lines and lines indicate the direction of microstructure (green: ±45°-oriented microstructures; red: vertically oriented microstructures). Orange and blue double lines indicate high angle grain boundary (HAGB) and low angle grain boundary (LAGB), respectively.

was not observed in the center part of the melt pool (Figs. 5(d), 5(h)). These observations suggest that the growth of the <001>-oriented crystal does not necessarily coincide with the heat flow direction.

One possible factor responsible for texture formation is interfacial energy, as it is closely related to crystal growth

and grains that minimize this energy are preferentially formed.[33] In the solidification process, interfacial energy decreases as the misorientation between adjacent grains is reduced. It is observed that HAGBs are formed at the interfaces between adjacent grains aligned along the z-axis and ±45° in the ±X-scan, as illustrated in Fig. 6(b), reflecting crystal growth governed by the heat flow direction. In contrast, in the case of ±X-brick-scan, ±45°-inclined solidification fronts migrating from the right and left halves of the melt pool encountered at the melt pool center and formed a fusion boundary as a LAGB along the z-axis (Fig. 5(d)), as illustrated in Fig. 6(c). This decreased the interfacial energy. Therefore, in the ±X-brick-scan, the <001> growth driven by the reduction of misorientation at the fusion boundary is considered to be more effective in lowering the overall interfacial energy of the system than the <001> growth along the heat flow direction. Thus, crystal growth direction in the L-PBF process is not solely dictated by heat flow but is significantly influenced by interfacial energy minimization.

4. Conclusions

This study demonstrates, for the first time, a single-crystalline-like $<011>_{//z}$-oriented texture in 316L SS, achieved using a newly designed ±X-brick-scan strategy in L-PBF. This strategy demonstrates that the crystal growth direction is governed not only by heat flow, but also by interfacial energy minimization. These findings highlight the potential of L-PBF as a powerful tool for tailoring crystallographic texture and the related functional properties of metallic materials.

Statement for Conflict of Interest

The authors declare no conflict of interest.

Acknowledgments

This work was partially supported by Grants-in-Aid for Scientific Research from the Japan Society for the Promotion of Science (JSPS) [grant number 23K23080 and 25K00051] and CREST-Nanomechanics: Elucidation of Macroscale Mechanical Properties based on Understanding Nanoscale Dynamics for Innovative Mechanical Materials ([grant number JPMJCR2194)] from the Japan Science and Technology Agency (JST). ISIJ Research Promotion Grant from the Iron and Steel Institute of Japan (ISIJ).

Nomenclature

G: Thermal gradient (K/m)
R: Solidification rate (m/s)
P: Laser power (W)
v: Scanning speed (mm/s)
d: Scanning pitch (mm)
t: Stacking thickness (mm)
ED: Energy density (J/mm^3)

REFERENCES

1) S. L. Sing and W. Y. Yeong: *Virtual Phys. Prototyp.*, **15** (2020), 359. https://doi.org/10.1080/17452759.2020.1779999
2) N. Ikeo, H. Fukuda, A. Matsugaki, T. Inoue, A. Serizawa, T. Matsuzaka, T. Ishimoto, R. Ozasa, O. Gokcekaya and T. Nakano: *Crystals*, **11** (2021), 959. https://doi.org/10.3390/cryst11080959
3) N. Ikeo, T. Matsumi, T. Ishimoto, R. Ozasa, A. Matsugaki, T. Matsuzaka, O. Gokcekaya, Y. Takigawa and T. Nakano: *Crystals*, **11** (2021), 1074. https://doi.org/10.3390/cryst11091074
4) A. Matsugaki, T. Matsuzaka, T. Mori, M. Saito, K. Funaoku, R. Yamano, O. Gokcekaya, R. Ozasa and T. Nakano: *Int. J. Bioprint.*, **10** (2024), 406. https://doi.org/10.36922/ijb.1425
5) X. Sheng, A. Guo and X. Lin: *J. Manuf. Process.*, **119** (2024), 179. https://doi.org/10.1016/j.jmapro.2024.03.081
6) J. Noronha, J. Dash and M. Qian: *Adv. Mater.*, **36** (2024), 2308715. https://doi.org/10.1002/adma.202308715
7) T. Ishimoto, K. Hagihara, K. Hisamoto, S.-H. Sun and T. Nakano: *Scr. Mater.*, **132** (2017), 34. https://doi.org/10.1016/j.scriptamat.2016.12.038
8) T. Todo, T. Ishimoto, O. Gokcekaya, J. Y. Oh and T. Nakano: *Scr. Mater.*, **206** (2022), 114252. https://doi.org/10.1016/j.scriptamat.2021.114252
9) K. Hagihara and T. Nakano: *J. Met.*, **74** (2022), 1760. https://doi.org/10.1007/s11837-021-04966-7
10) M. T. Andani, Z. Zhang, V. Sundararaghavan and A. Misra: *J. Mater. Res. Technol.*, **30** (2024), 7375. https://doi.org/10.1016/j.jmrt.2024.05.086
11) C. Sofras, J. Capek, C. Leinenbach and E. Polatidis: *Virtual Phys. Prototyp.*, **19** (2024), e2390483. https://doi.org/10.1080/17452759.2024.2390483
12) Y. Wang, B. Wang and H. Fu: *Scr. Mater.*, **239** (2024), 115806. https://doi.org/10.1016/j.scriptamat.2023.115806
13) T. Ishimoto, R. Ozasa, K. Nakano, M. Weinmann, C. Schnitter, M. Stenzel, A. Matsugaki, T. Nagase, T. Matsuzaka, M. Todai, H. S. Kim and T. Nakano: *Scr. Mater.*, **194** (2021), 113658. https://doi.org/10.1016/j.scriptamat.2020.113658
14) Y. S. Kim, O. Gokcekaya, K. Sato, R. Ozasa, A. Matsugaki and T. Nakano: *Mater. Des.*, **252** (2025), 113824. https://doi.org/10.1016/j.matdes.2025.113824
15) N. Ren, J. Li and J. Li: *Nat. Commun.*, **14** (2023), 7990. https://doi.org/10.1038/s41467-023-43563-x
16) H. Amano, T. Ishimoto, R. Suganuma, K. Aiba, S.-H. Sun, R. Ozasa and T. Nakano: *Addit. Manuf.*, **48** (2021), 102444. https://doi.org/10.1016/j.addma.2021.102444
17) H. Chen, D. Egusa, Z. Li, T. Sasaki, R. Ozasa, T. Ishimoto, M. Okugawa, Y. Koizumi, T. Nakano and E. Abe: *Addit. Manuf.*, **102** (2025), 104737. https://doi.org/10.1016/j.addma.2025.104737
18) Y. Yamabe-Mitarai, T. Inoue, T. Kuroda, S. Matsunaga, Y. Toda, T. Matsunaga, T. Ito, R. Ozasa, T. Ishimoto and T. Nakano: *Mater. Trans.*, **64** (2023), 1175. https://doi.org/10.2320/matertrans.MT-ME2022010
19) S.-H. Park, O. Gokcekaya, R. Ozasa, M.-H. Oh, Y.-W. Kim, H. S. Kim and T. Nakano: *Met. Mater. Int.*, **30** (2023), 1227. https://doi.org/10.1007/s12540-023-01579-4
20) Y. S. Kim, O. Gokcekaya, A. Matsugaki, R. Ozasa and T. Nakano: *Materialia*, **38** (2024), 102241. https://doi.org/10.1016/j.mtla.2024.102241
21) P. V. Cobbinah, S. Matsunaga, Y. Toda, R. Ozasa, M. Okugawa, T. Ishimoto, Y. Liu, Y. Koizumi, P. Wang, T. Nakano and Y. Yamabe-Mitarai: *Smart Mater. Manuf.*, **2** (2024), 100050. https://doi.org/10.1016/j.smmf.2024.100050
22) W. Xu, M. Brandt and M. Qian: *Acta Mater.*, **85** (2015), 74. https://doi.org/10.1016/j.actamat.2014.11.028
23) J. Al-Lami, T. Dessolier and M. Pham: *Adv. Eng. Mater.*, **27** (2025), 2400524. https://doi.org/10.1002/adem.202400524
24) Y. S. Li, L. Q. Cui and W. F. He: *Int. J. Plast.*, **191** (2025), 104379. https://doi.org/10.1016/j.ijplas.2025.104379
25) R. Ozasa, A. Matsugaki, T. Ishimoto and T. Nakano: *Mater. Trans.*, **64** (2023), 31. https://doi.org/10.2320/matertrans.MT-MLA2022011
26) S.-H Sun, T. Ishimoto, K. Hagihara, Y. Tsutsumi, T. Hanawa and T. Nakano: *Scr. Mater.*, **159** (2019), 89. https://doi.org/10.1016/j.scriptamat.2018.09.017
27) T. Ishimoto, S. Wu, Y. Ito, S.-H. Sun, H. Amano and T. Nakano: *ISIJ Int.*, **60** (2020), 1758. https://doi.org/10.2355/isijinternational.ISIJINT-2019-744
28) Y. Tsutsumi, T. Ishimoto, T. Oishi, T. Manaka, P. Chen, M. Ashida, K. Doi, H. Katayama, T. Hanawa and T. Nakano: *Addit. Manuf.*, **45** (2021), 102066. https://doi.org/10.1016/j.addma.2021.102066
29) Z. Que, L. Chang, T. Saario and M. Bojinov: *Addit. Manuf.*, **60** (2022), 103205. https://doi.org/10.1016/j.addma.2022.103205
30) S.-B. Shin, S.-J. Song, Y.-W. Shin, J.-G. Kim, B.-J. Park and Y.-C. Suh: *Mater. Trans.*, **57** (2016), 2116. https://doi.org/10.2320/matertrans.M2016222
31) B. Sun, X. Zuo, X. Cheng and X. Li: *npj Mater. Degrad.*, **4** (2020), 37. https://doi.org/10.1038/s41529-020-00142-5
32) J. A. Dantzig and R. Michel: Solidification, 2nd Ed., EPFL Press, Lausanne, (2016), 69. ISBN978-2940222971
33) T. Ishimoto, N. Morita, R. Ozasa, A. Matsugaki, O. Gokcekaya, S. Higashino, M. Tane, T. Mayama, K. Cho, H. Y. Yasuda, M. Okugawa, Y. Koizumi, M. Yoshiya, D. Egusa, T. Sasaki, E. Abe: *Acta Mater.*, **286** (2025), 120709. https://doi.org/10.1016/j.actamat.2025.120709